Systematic study of packaging designs on the performance of CMOS thermoresistive micro calorimetric flow sensors

Wei Xu[1], Liang Pan[2], Bo Gao[1], Yi Chiu[3], Kun Xu[1] and Yi-Kuen Lee[1,4]

[1] Hong Kong University of Science and Technology, Hong Kong, People's Republic of China
[2] Institute of Applied Physics and Computational Mathematics, Beijing, People's Republic of China
[3] National Chiao Tung University, Hsinchu, Taiwan

E-mail: meyklee@ust.hk

Abstract

We systematically study the effect of two packaging configurations for the CMOS thermoresistive micro calorimetric flow (TMCF) sensors: S-type with the sensor chip protrusion-mounted on the flow channel wall and E-type with the sensor chip flush-mounted on the flow channel wall. Although the experimental results indicated that the sensitivity of the S-type was increased by more than 30%; the corresponding flow range as compared to the E-type was dramatically reduced by 60% from 0–11 m s^{-1} to 0–4.5 m s^{-1}. Comprehensive 2D CFD simulation and in-house developed 3D numerical simulations based on the gas-kinetic scheme were applied to study the flow separation of these two packaging designs with the major parameters. Indeed, the S-type design with the large protrusion would change the local convective heat transfer of the TMCF sensor and dramatically decrease the sensors' performance. In addition, parametric CFD simulations of the packaging designs provide inspiration to propose a novel general flow regime map (FRM), i.e. normalized protrusion d^* versus reduced chip Reynolds number Re^*, where the critical boundary curve for the flow separation of TMCF sensors was determined at different channel aspect ratios. The proposed FRM can be a useful guideline for the packaging design and manufacturing of different micro thermal flow sensors.

Keywords: micro calorimetric flow sensors, CMOS MEMS, flow separation, CFD simulation, flow regime map, gas-kinetic scheme

(Some figures may appear in colour only in the online journal)

Introduction

After the first reported silicon-based micro flow sensor in 1974 [1], many micro thermal flow sensors based on different principles have been presented for various fluids [2–5]. These thermal flow sensors demonstrated diverse applications in biomedical instrumentation, environmental monitoring, and microfluidic devices. Comprehensive research studies

of the flow sensor's packaging will be necessary to achieve accurate flow measurements. Otherwise, the improper packaging design of the flow sensor will lead to inaccurate flow measurements due to the leakage, or a dramatically reduced sensor performance caused by the flow separation or turbulence [6, 7].

In general, monolithically integrated flow channels within the sensor chip or the post integrated housing structure were adopted to build up the flow measurement system. In comparison with the monolithic integration approach, the introduction of the housing requires less wafer area and provides a flexible design with the adjustable flow rates. To date, the CMOS

---

[4] Author to whom any correspondence should be addressed.
Department of Mechanical and Aerospace Engineering, Hong Kong University of Science and Technology, Clear Water Bay, Kowloon, Hong Kong, People's Republic of China.
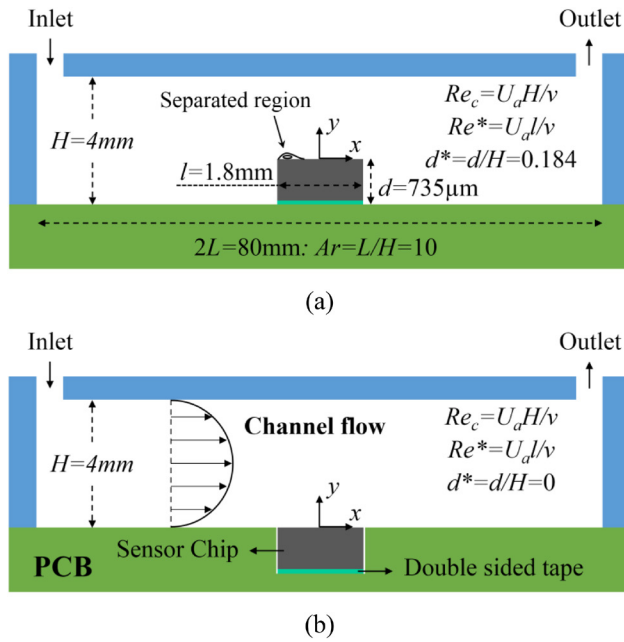
Figure 1. Parameter study of the TMCF sensor responses to two packaging designs: (a) stand-up packaging design (S-type, $d^* = 0.184$), (b) embedded packaging design (E-type, $d^* = 0$). U_a is the average flow velocity in the main flow channel.

MEMS technologies have been gradually adopted to implement the microsensors with the on-chip microelectronics [8–10]. To reduce the expensive chip area in the CMOS fabrication process, the employment of housing structure in the thermal flow sensor packaging is a practical solution.

Different housing concepts for the packaging of thermal flow sensors were reported [11–13], such as the surface mounted adaptor on the chip, the sealed flow channel with a chip or a part of chip inside, and the flipping housing design. However, very few works have systematically studied the effect of packaging design on the performance of micro thermal flow sensors. Recently, Dumstorff *et al* [6] reported a sensor packaging design with a portion of sensor chip inside the flow channel and observed the decrease of sensitivity in the non-flushed sensor packaging compared to the flush-mounted counterpart.

In this work, we first investigate the responses of our CMOS thermoresistive micro calorimetric flow (TMCF) sensors with two different packaging designs in the Poly(methyl methacrylate) (PMMA) flow channel: S-type and E-type as shown in figure 1 [7]. Although the experimental results indicated that the sensitivity of S-type in the low-speed input flow was increased, its flow range as compared to the E-type was dramatically reduced. The characteristic curves of TMCF sensors in these two designs were studied and explained. To improve the proposed flow regime map [7] for the design of sensor packaging, the comprehensive numerical studies on the TMCF sensors with different protrusion ratio d^* and channel aspect ratio Ar were conducted.

While the fluid flow in the PMMA channel is fully attached, the flow over the packaged TMCF sensors can be either separated or attached [14]. In this paper, a reduced chip Reynolds

number Re^* was used to characterize the flow separation, as shown in equation (1).

$$Re^* = U_a l / \nu \qquad (1)$$

where U_a is the average flow velocity in the main flow channel, l is the length of TMCF sensor chip, and ν is the kinematic viscosity. As stated, to study the geometry effect on the packaged TMCF sensors, the protrusion ratio d^* is defined as:

$$d^* = d / H \qquad (2)$$

where d is the protrusion height of TMCF sensor, and H is the height of flow channel. On the other hand, the channel aspect ratio Ar is defined as:

$$Ar = L / H \qquad (3)$$

where L is the half-length of the flow channel.

Fabrication and packaging of TMCF sensors

As shown in figure 2(a), we applied our 1D sensor model [15, 16] to design and fabricate the TMCF sensors by using a commercial 0.35 μm 2P4M CMOS MEMS process that followed an alike post-CMOS process in [17]. The TMCF sensor consists of a Poly-Si resistive micro heater (R_h) at the center of the thin film and three pairs of symmetrically located upstream (R_u) and downstream (R_d) thermoresistive sensors with the different distance from the micro heater, $D = 60$ μm (Pair 1), 120 μm (Pair 2), 180 μm (Pair 3). In the presence of fluid flow, the differential temperature output ΔT_{out} of TMCF sensor between the upstream (R_u) and the downstream (R_d) sensors is related to the convective heat transfer and namely the corresponding input fluids flow velocity U. With the integration of R_u and R_d into a Wheatstone bridge, the thermal output ΔT_{out} can be converted to an electrical voltage signal V_{out} for the practical flow sensing [18].

The detailed microfabrication processes of TMCF sensor could be found elsewhere [15, 16]. Herein, we only briefly describe the key fabrication steps. The micro heater R_h has a 250 μm × 100 μm Poly-Si serpentine structure with a width of 10 μm, and the measured average resistance is 1407 Ω at the room temperature of 22.5 °C. Three pairs of thermoresistive upstream and downstream sensors also have an identical 250 μm × 18 μm Poly-Si serpentine structure with a width of 2 μm, where the measured average resistance is 5478 Ω. To improve the sensitivity of TMCF sensor with the reduced conductive heat loss, the 600 μm × 400 μm suspended thermally low-conducting thin-film structure was constructed through the combined selective oxide reactive-ion etching (RIE) and the XeF$_2$ isotropic Si etching. It is worthwhile noting that the CMOS fabrication process and the mechanical strength of the thin film materials limit the thickness of the thin film.

Figure 2(b) shows the packaged TMCF sensor, where the finally diced sensor chip with the remained safety clearance to the sensor layout has a size of 1.8 mm × 1.8 mm × 0.65 mm (Length × Width × Height). The TMCF sensor chips were attached to a PCB board with an 85 μm thick double-sided tape
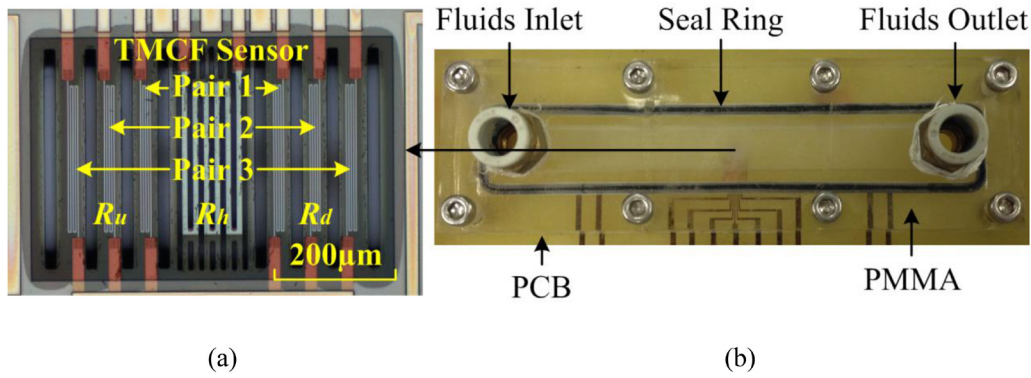
Figure 2. (a) Fabricated and (b) packaged TMCF sensors in the PMMA flow channels.
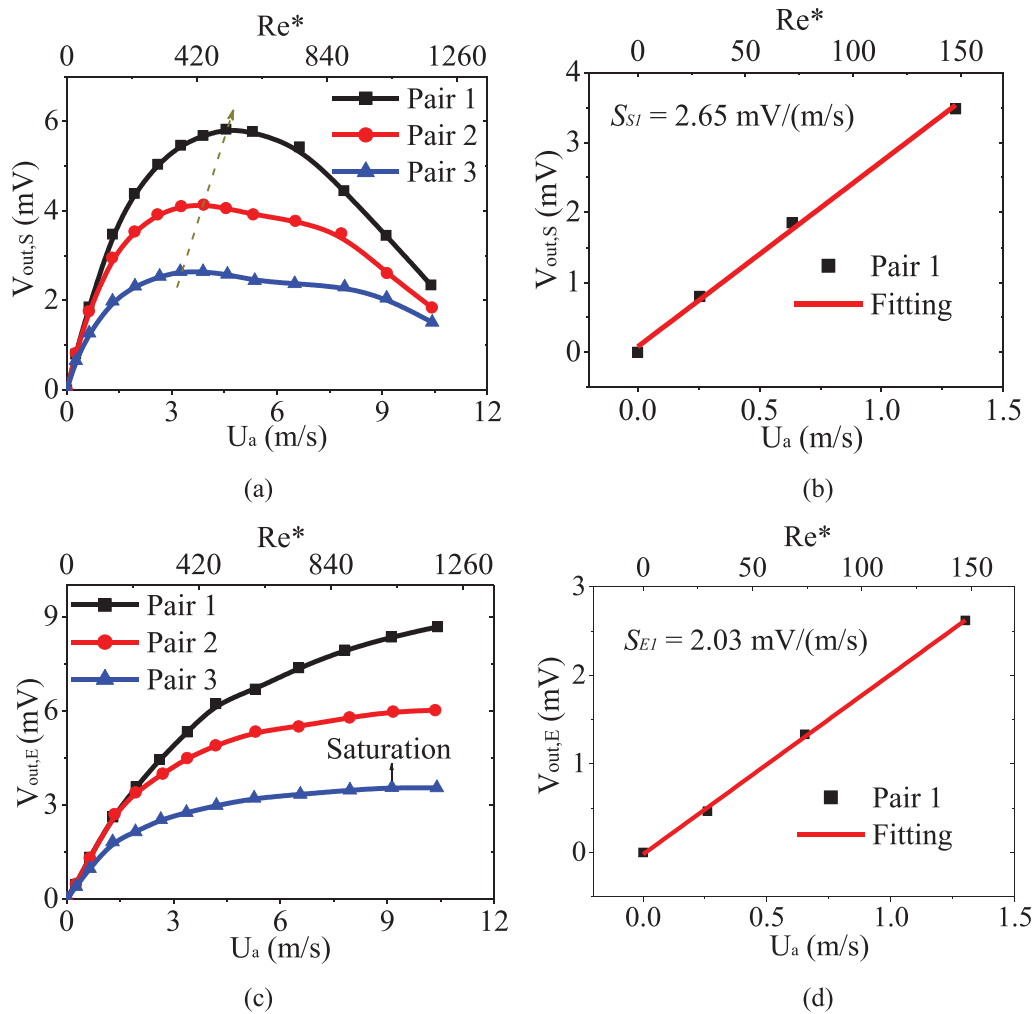

Figure 3. The output voltage V_{out} of the TMCF sensors with two packaging designs versus the input flow velocity in the 3 mA constant current (CC) mode: (a) S-type's $V_{out,S}$ (U_a), (b) close-up view of the S-type's $V_{out,S}$ (U_a), (c) E-type's $V_{out,E}$ (U_a), (d) close-up view of the E-type's $V_{out,E}$ (U_a). Note, the sensitivity is determined by the curve's slope at the zero input flow velocity.

and packaged into the center of an $80\,mm \times 8\,mm \times 4\,mm$ (Length × Width × Height) PMMA flow channel with two designs: i.e. E-type and S-type, as shown in figure 1. Note, for the comparison between E-type and S-type, the coordinate system is placed at the center of TMCF sensors' surface. The packaged TMCF sensors were then tested with the nitrogen gas flow, where the detailed experimental setup was described elsewhere [7].

Experimental results of TMCF sensors

The measured output and sensitivity of S-type and E-type TMCF sensors with the micro heater (R_h) working on 3 mA constant current (CC) mode are plotted against the input N_2 gas flow from 0 m s^{-1} to 11 m s^{-1} as shown in figure 3. The electrical voltage output V_{out} of three pairs of TMCF sensors were directly measured from the upstream (R_u) and downstream (R_d)

thermoresistive resistors with the Wheatstone bridge-based interface circuit. In the low flow region, the S-type TMCF sensors could achieve a larger output and higher sensitivity than that of E-type. Obviously, a higher sensitivity ($S_{S1} = 2.65$ mV (m s^{-1})$^{-1}$) of Pair 1 TMCF sensor in S-type was achieved as compared to the counterpart in E-type ($S_{E1} = 2.03$ mV (m s^{-1})$^{-1}$), as shown in figures 3(b) and (d), respectively. Similarly, from the linear fitting of sensor response at the low-speed input gas flow, both Pair 2 and Pair 3 TMCF sensors in the S-type showed the higher sensitivity of $S_{S2} = 2.44$ mV (m s^{-1})$^{-1}$ and $S_{S3} = 1.96$ mV (m s^{-1})$^{-1}$ than those of E-Type ($S_{E2} = 2.02$ mV (m s^{-1})$^{-1}$ and $S_{E3} = 1.52$ mV (m s)$^{-1}$)$^{-1}$, respectively. However, the flow range of S-type was dramatically reduced by more than 60%, as shown in figures 3(a) and (c), respectively. Moreover, the output voltage of the S-type design can easily reach saturation when the temperature sensors were further placed from the microheater (R_h), i.e. the flow range of Pair 3 < Pair 2 < Pair 1.

Note that, the non-monotonic behavior of the Pair 3 TMCF sensor in the E-type was observed, which was saturated at 9 m s^{-1}. For the high-speed input gas flow (>9 m s^{-1}), both the heater and temperature sensors would experience an enhanced overall cooling effect due to the reduced thermal boundary layer δ_t, which resulting in a saturated TMCF sensor response. The boundary layer effect does impose the non-monotonic behavior of the calorimetric flow sensors, where the detailed studies could be found in the work of Elwenspoek and Wiegerink [19]. The maximum sensor output occurred at the condition of thermal boundary layer δ_t roughly equivalent to the distance D between the heater and sensor, which could be used to describe the non-monotonic behavior in the TMCF sensors. The δ_t over the TMCF sensor chip is inversely proportional to the root mean square of input fluid flow U [20]. Therefore, we can roughly estimate a 5% reduction of the flow range in the S-type design compared to the E-Type by considering the averaged flow velocity over the sensor chip. Moreover, the detailed 1D and CFD design analysis for the Pair 2 TMCF sensor in [15, 16] has shown the accessible flow range larger than 10 m s^{-1} under the open-space flow condition (belongs to S-Type sensor with the fluid flow over the TMCF sensor's surface begins at the leading edge of sensor chip, which resulted in the smallest δ_t for the same input flow). Therefore, regarding the dramatically reduced flow range (more than 60%) of the S-Type TMCF sensor, the inherent non-monotonic behavior is not the critical issue and therefore was ignored in this paper. There should be one dominating cause for this dramatically reduced flow range in the S-Type TMCF sensor, which will be revealed in the following section.

Results and discussion

Two-dimensional CFD simulations (CFDRC, ESI Group, France) were first performed to investigate the discrepancy of TMCF sensors' response between the S-type and the E-type. The preliminary simulation results showed that the N$_2$ gas flow in the bottom cavity of TMCF sensors could be ignored due to the sparse opening of the thin film structure.

Therefore, for the ease of meshing and modeling, the cross section of TMCF sensor chip in S-type was approximated as a solid rectangular domain with $l = 1.8$ mm and $d = 735$ μm. A total number of 805 195 cells were created in the simulation domain with the locally refined mesh model around the TMCF sensor as shown in figure 4(a). Here, the numerical simulation only employs the fluid mechanics module of CFD-ACE (CFDRC, ESI Group). Note that, in both simulation domain and experimental condition, the length L between the inlet and the TMCF sensor is 40 mm, which leads to a channel aspect ratio Ar = 10 as shown in figure 4(a). The flow patterns over the E-type and S-type TMCF sensors under the 1 m s^{-1} input nitrogen gas flow were plotted in figures 4(b) and (c), where the velocity profile over the E-type TMCF sensor was close to the fully developed flow. Figure 4(d) showed the increase of local flow velocity U and also the wall shear stress $\tau_w = \eta(\partial U/\partial y)|_{\text{surface}}$ in the S-type TMCF sensor, where a thinner momentum boundary layer δ (well visible in the figure 4(d)) than that of E-type was developed. Note, although the simplified 2D simulation with the employment of fluid mechanics was performed, the qualitative explanation for the enhanced sensitivity in S-type TMCF sensor could be given with the increased momentum boundary layer δ or the more straightforward thermal boundary layer $\delta_t \sim \delta/\text{Pr}^{1/3}$.

As shown in figure 4(d), the velocity gradient in the S-Type along the y axis is higher than that of E-Type, which presented a larger shear stress τ_w over the sensor chip, i.e. $\tau_{w\text{-S}} > \tau_{w\text{-E}}$. The τ_w is inversely proportional to the momentum boundary layer δ, also to the thermal boundary layer δ_t [19]. Therefore, for $\tau_{w\text{-S}} > \tau_{w\text{-E}}$, the thickness of δ_t in S-Type sensor was thinner than that of E-Type, hence, an overall enhanced convection heat transfer (often characterized by the Nusselt number Nu) was expected, where the increased sensor output and sensitivity in S-Type TMCF sensor were predictable at the small input flows. Moreover, with the thinner developed local momentum boundary layer δ_x that especially close to the leading edge, the upstream temperature sensor experienced a larger local shear stress $\tau_{w\text{-S:u}}$ than the downstream one $\tau_{w\text{-S:d}}$. Considering the heat transfer behavior over an isothermal plate [20] in the S-type TMCF sensor, the local Nusselt number (Nu$_x$) as a function of Reynold number (Re$_x$) or the shear stress τ_{wx} in equation (4), could be used to qualitatively explain the local heat transfer behavior difference in the TMCF sensors packaging.

$$\text{Nu}_x = 0.332\text{Pr}^{1/3}\text{Re}_x^{1/2} \propto \frac{1}{\delta_{tx}} \propto \frac{1}{\delta_x} \propto \tau_{wx}^{1/3} \qquad (4)$$

where Pr is the Prandtl number defined as the ratio of the momentum diffusivity of the working fluid (N$_2$) to the thermal diffusivity, and Re$_x$ is:

$$\text{Re}_x = U(x + 0.5l)/\nu. \qquad (5)$$

Equation (4) reveals that the heat transfer difference between the upstream Nu$_u$ and the downstream Nu$_d$ was increased with the increased flow velocity U or the shear stress τ_w. As the upstream temperature sensor experienced a larger local shear stress $\tau_{w\text{-S:u}}$ than the downstream one $\tau_{w\text{-S:d}}$, hence, the heat transfer difference was further increased especially due to the
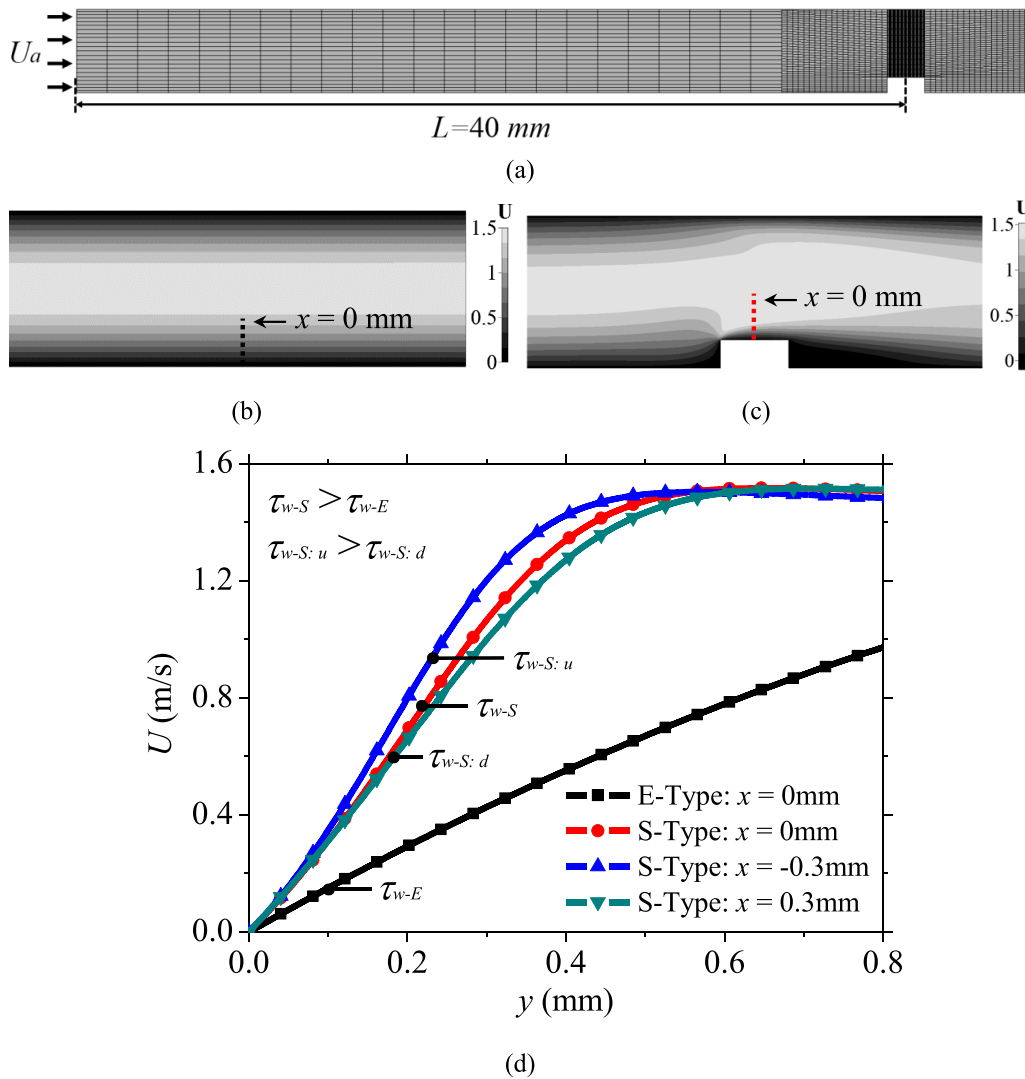
Figure 4. (a) The numerical model of S-type design with 805 195 cells (not to the scale). The developed flow pattern under the average input flow velocity $U_a = 1$ m s^{-1} in (b) E-type, (c) S-type, (d) comparison of the local flow velocity U over the center of the TMCF sensor ($x = 0$ mm). Note: Ar = 10, and the velocity profile over the E-type was close to the fully developed laminar flow [14].

enhanced local heat transfer Nu$_u$ from the upstream sensor, which explains the significantly increased output and sensitivity of S-type TMCF sensor under the low-speed input N$_2$ gas flow.

For a blunt sensor chip immersed into the streamlined fluid flow, the flow separation is unavoidable at high Reynolds flow. The generated flow separation will significantly change the TMCF sensor's performance that will be elaborated in the following 2D and 3D CFD simulation. The 3D CFD simulation is based on the gas-kinetic scheme that both fluid mechanics and the effect of heat transfer was considered in the numerical simulations at the same time [21, 22]. More detailed CFD simulations with the coupled fluid mechanics and heat transfer for the quantitative analysis of the performance changes in E-Type and S-Type will be studied in the future work. Considering the fluid flow over the surface ($y = 0$ mm) of TMCF sensor, the separated flow can be determined by the condition of the negative velocity gradient, equation (6) [14]:

$$\partial U / \partial y \,|_{\text{surface}} \leqslant 0. \tag{6}$$

Figure 5(a) showed that an adverse pressure gradient is generated when the gas flow approaches the S-type sensor under the 7 m s^{-1} input N$_2$ flow. In general, the effect of an adverse pressure gradient will lead to the decrease of flow velocity in the streamwise direction. If this undesired pressure gradient acts on the surface over a sufficient distance, we would observe a separated flow over the TMCF sensor, especially in the upstream area. As shown in figure 5(b), a reduced or even reversed gas flow (-0.1 m s^{-1}) near the upstream area of TMCF sensor is observed, in which, a local velocity profile along the y direction at $x = -0.65$ mm is plotted in figure 5(c).

According to equation (4), the reduced or reversed gas flow ($\tau_w < 0$) at upstream would lead to a dramatically decreased local Nusselt number Nu$_u$. As shown in figures 5(b) and (d), the reattached gas flow at the surface of the S-Type TMCF sensor occurred before the center (micro heater) of the sensor die. Therefore, the gas flow was fully attached at the downstream area of the TMCF sensor without the significant flow separation; then an enhanced downstream Nu$_d$ is still expected. Therefore, the difference between the upstream Nu$_u$

(a)   (b)

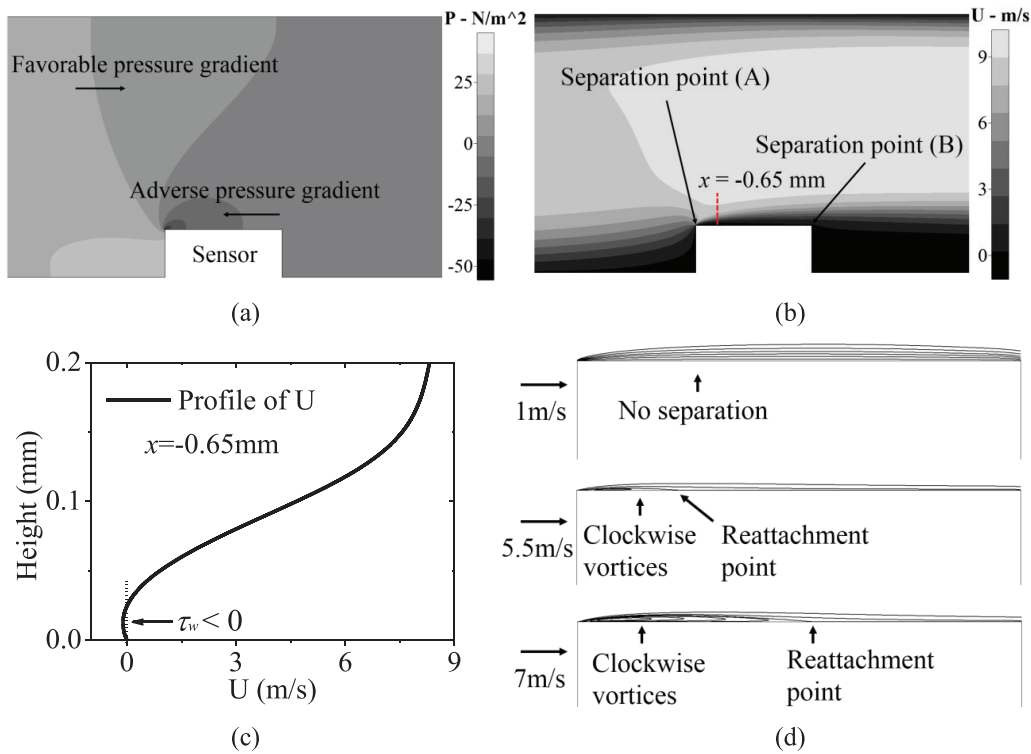(c)   (d)

Figure 5. (a) Pressure distribution, (b) flow separation due to the adverse pressure gradient and (c) local velocity profile on the separated flow region ($x = -0.65$ mm) under the uniform input flow velocity $U_a = 7$ m s^{-1}, (d) comparison of streamline over the sensor chip under the uniform input flow velocity $U_a = 1$ m s^{-1}, 5.5 m s^{-1} and 7 m s^{-1}, respectively. Note: Ar = 10.

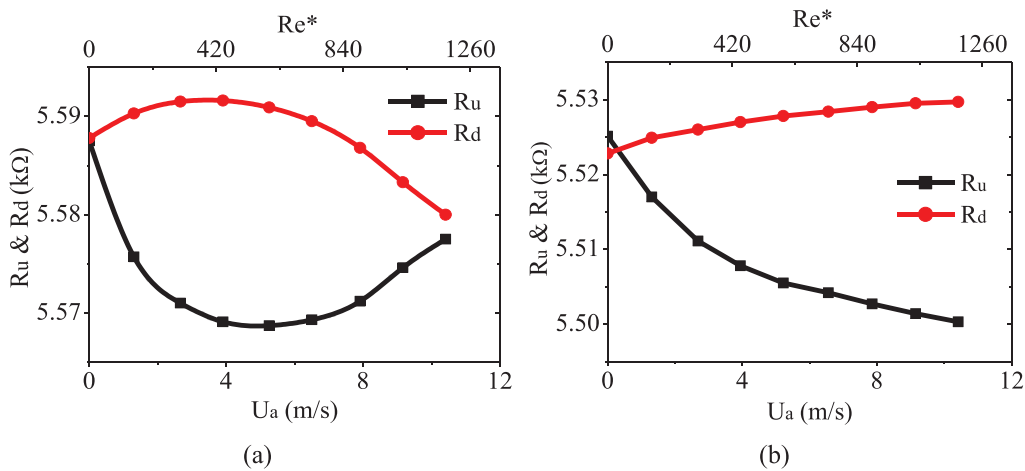(a)   (b)

Figure 6. The measured resistance changes of upstream R_u and downstream R_d in pair 1 TMCF sensor: (a) S-type and (b) E-type.

and the downstream Nu_d is decreased under the high-speed flow, which leads to a decreased output voltage in the S-type sensor. In addition, figure 5(d) shows an enlarged flow separation region with the increased input gas flow. Therefore, the flow range of the S-type TMCF sensor will become smaller when the thermoresistive sensors are placed at the location further away from the micro heater.

For an even higher input flow, the separated flow region may cover three pairs of TMCF sensors in both upstream and downstream area, and the negative vortex flow over the TMCF sensors may eventually lead to a negative sensor response. The possibility of generated negative outputs in these three pairs of TMCF sensors is revealed by the tendency of sensors'

response curves at 11 m s^{-1} as shown in figure 3(a). Note that, due to the limited flow range of reference flow meter, the tested flow range of S-Type and E-Type TMCF sensors were from 0 m s^{-1} to 11 m s^{-1}. However, this predictable negative TMCF sensors' response could be validated by a wind tunnel testing with the input air flow from 0.14 m s^{-1} to 19 m s^{-1}, where the TMCF sensor chip was mounted on the center of a 4.4 mm width wedge-shaped PCB board.

The resistance changes of Pair 1's upstream (R_u) and downstream (R_d) sensors were plotted as a function of average input flow velocity U_a and the reduced chip Reynolds number Re* for S-type and E-type sensors, respectively; as shown in figure 6. For the S-type sensor, the resistance of R_u is firstly
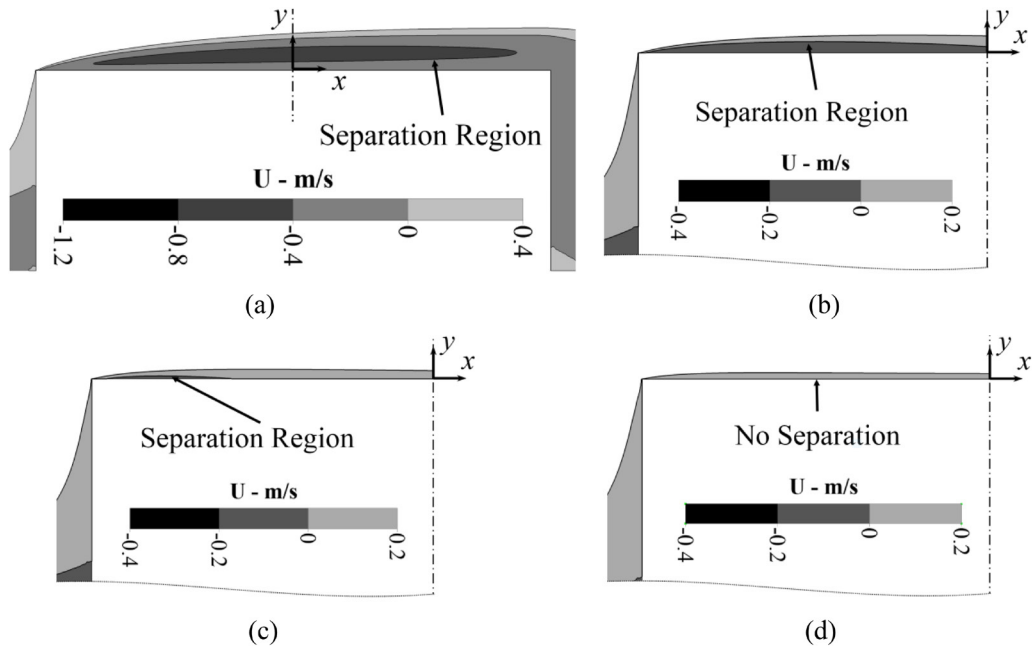
Figure 7. Simulated negative velocity profiles over the TMCF sensor chip ($d^* = 0.175$) under the uniform input flow of 6 m s^{-1} with the different channel aspect ratio: (a) Ar = 1.5, (b) Ar = 4, (c) Ar = 10, (d) Ar = ∞.

decreased and then inversely increased with the increased gas flow; while the resistance of R_d is slightly increased and then decreased. For the E-type sensor design, the resistance of R_u is monotonously decreased with the increased input flow due to the enhanced heat convection, while the resistance R_d is slightly increased due to the transferred thermal energy from R_h. By comparing the sensors' resistance change especially for R_u between the S-type and the E-type as shown in figure 6, the results demonstrated that the flow over the surface of S-type would become separated under the condition of high-speed input flow.

Previously, based on the 2D CFD simulations, we built a flow regime map (protrusion d^* versus reduced chip Reynolds number Re*) with the boundary between different flow patterns (separated flow and attached flow) over the TMCF sensors [7]. Later, we realized that in our flow channel packaged designs; the TMCF sensors are most likely located in the entrance region with the fluid flow under developing, especially for the high-speed input flow. In this case, the determination of flow separation is influenced by the leading length L or Ar due to the different developed flow profiles at the sensor location.

Herein, a series of 2D CFD simulations for S-type TMCF sensors ($d^* = 0.175$) with the different channel aspect ratio Ar = 1.5, 4, 10 and ∞ were conducted under the 6 m s^{-1} input N$_2$ gas flow. The simulated negative U profiles are plotted in figure 7, where the observed local velocity profiles over the TMCF sensors are quite different. The whole TMCF sensor is covered by a separated flow with the Ar = 1.5 ($L = 6$ mm) as shown in figure 7(a), while the separated flow region (left side plotted) is gradually diminished with the increased Ar as shown in figures 7(b) and (c). Moreover, for Ar = ∞, there is no flow separation occurred in the TMCF sensors as shown in figure 7(d). Note, for the case of infinite aspect ratio Ar, the fully developed parabolic velocity profile is set at the inlet of CFD models [14]. The negative gas flow profiles in figure 7

clearly show that the channel aspect ratio Ar plays an important role in the determination of flow separation.

The flow separation phenomenon in figure 7 can be qualitatively explained by the developed boundary layer along the flow channel. Let us consider a uniform fluid flow, which begins at the inlet, enters the flow channel; a thin viscous boundary layer will be generated and then gradually grows along the flow channel until the viscous stresses dominate the entire cross section. Similar to the laminar fluid flow over a plate, the developed boundary layer thickness [20] at the TMCF sensor location can be approximately calculated as:

$$\delta_x = 4.64\sqrt{\frac{\nu L}{U}}. \tag{7}$$

Equation (7) shows that the boundary layer thickness δ_x is increased with L, and its maximum value will be $0.5H$ when the flow is fully developed. Figure 8 shows the normalized boundary layer thickness d/δ_x plotted as a function of channel aspect ratio Ar under the 6 m s^{-1} input flow. For shorter Ar, the TMCF sensor stands above the boundary layer, and a free stream approaching flow over the sensor chip could be expected. While for larger Ar, the boundary layer is much thicker than the protrusion height d, the TMCF sensor is immersed deeper into the boundary layer, and the significant viscous flow is expected. With the TMCF sensor inside the boundary layer, the approached fluid flow is expected to be dominated by viscosity and experienced a larger drag force from the sensor chip, which makes it much harder to generate the flow separation.

Based on the 2D CFD simulations, the flow region map for the S-type sensor ($d^* = 0.175$) with the effect of Ar is plotted in figure 9, in which, the required half-channel length L_f for the fully-developed laminar flow at the sensor location is described as follows [14]:
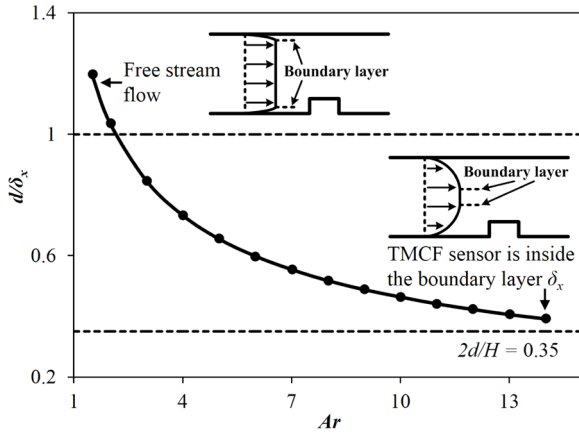
Figure 8. The developed boundary layer thickness (d/δ_x) as a function of channel aspect ratio Ar under the uniform input flow of 6 m s^{-1}. Note: $d^* = 0.175$.
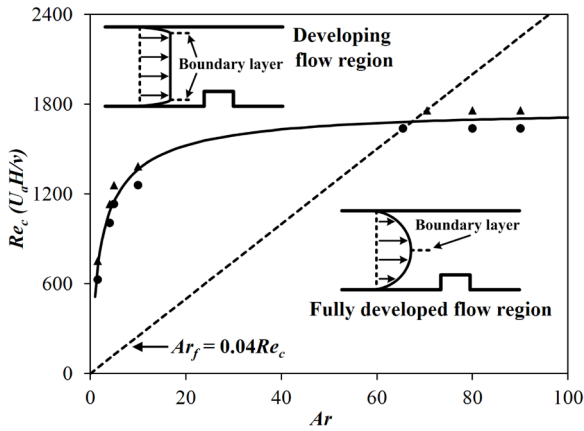

Figure 9. Flow regime map indicating the separated flow over the TMCF sensor chip ($d^* = 0.175$) based on the normalized parameters of Ar and Re_c (U_aH/ν); attached flow (circles), separated flow (triangles).

$$Ar_f = L_f/H = 0.04Re_c \qquad (8)$$

where the channel Reynold number is defined as $Re_c = U_aH/\nu$. Clearly, in the developing flow region, the flow separation can easily occur with the smaller Ar. The criterion for distinguishing the flow separation in the developing flow region is fitted with the CFD data and plotted as a solid line in figure 9, where its formula is described in equation (9). To obtain equation (9) to describe Re_c as a function of Ar, we first employed the curve fitting subroutine, 'nonlinear least square' with the algorithm of 'trust-region-reflective' algorithm in Matlab with the data points from the CFD simulations. The result of this subroutine shows that a general rational function, of which both numerator and denominator have the same degree of 1, could lead to a good fitting. Therefore, we amended the rational function with an additional term of $Re_c - 25Ar$ as shown in equation (9), where the right Re_c term would approach the fully developed parameter $Re_{c\,(Ar=\infty)}$ when Re_c increases to 25Ar.

$$\frac{1684}{Re_c} = 1 + 0.002\frac{Re_c - 25Ar}{Ar - 0.575}; \quad \begin{pmatrix} Re_c - 25Ar > 0 \\ Re_{c(Ar=\infty)} = 1684 \end{pmatrix} \qquad (9)$$
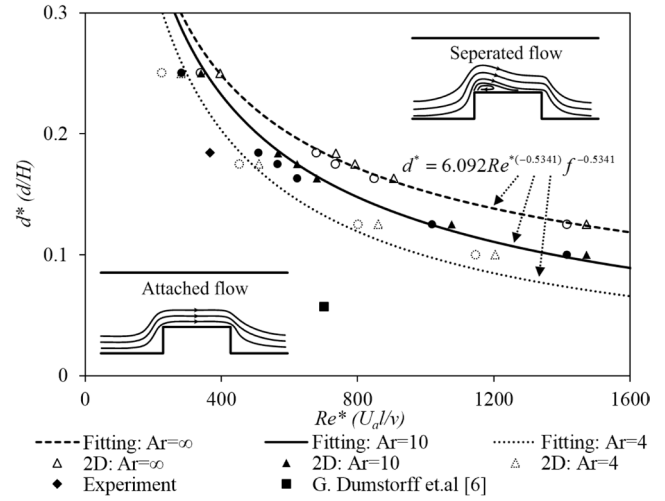

Figure 10. 2D Flow regime map indicating the separated flow over the sensor chip based on the normalized parameters d^* and Re^* with different Ar; attached flow (circles), separated flow (triangles).

A series of CFD simulations for S-type TMCF sensors with different protrusion height d^* were conducted under the condition of infinite $Ar = \infty$. Note the infinite Ar could be realized with the setting of parabolic velocity profile at the inlet of CFD model. Therefore, a clean data with the decoupled entrance effect is obtained. According to equation (6), a flow regime map (protrusion d^* versus reduced chip Reynolds number Re^*) with the distinct boundary between different flow patterns (separated flow and attached flow) over the TMCF sensor is plotted with the dashed line as shown in figure 10. The expected flow range of TMCF sensor with the infinite Ar can be dramatically reduced when the flow separation occurs if the followed criterion is met:

$$d^* = 6.092Re^{*(-0.5341)}. \qquad (10)$$

However, in the experimental condition, under the high Re_c flow, the TMCF sensors are located in the developing flow region. Therefore, additional simulation for the channel aspect ratio $Ar = 10$ and $Ar = 4$ with different d^* are conducted. As revealed in the above analysis, in these CFD simulations, the experimental condition of the TMCF sensor packaging involves the coupled phenomenon of flow separation under the effect of both the protrusion height d^* and the channel aspect ratio Ar. To address these two issues, the right term f in equation (9) is used to amend the equation (10) with the underlying physics.

$$d^* = 6.092Re^{*(-0.5341)}f^{-0.5341} \qquad (11)$$

where

$$f = 1 + 0.002\frac{Re_c - 25Ar}{Ar - 0.575}; \quad Re_c - 25Ar > 0$$
$$f = 1; \qquad\qquad\qquad Re_c - 25Ar \leqslant 0. \qquad (12)$$

As shown in figure 10, the new criterion in equation (11) could successfully distinguish the cases of separated flow and attached flow with different d^* and Ar. In addition, the reported experimental result of the step-up design (see the solid square symbol in figure 10) from the work of Dumstorff and the co-works [6]. is also plotted. As shown in the flow regime map,
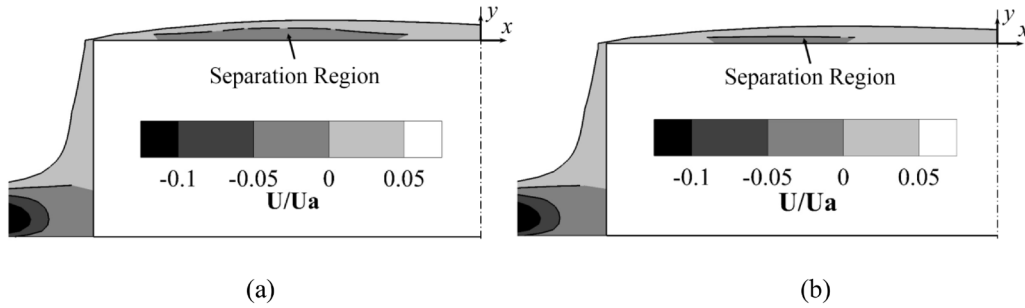
(a)

(b)

Figure 11. 3D Simulated negative velocity profile over the TMCF sensor chip (note: $d^* = 0.11$) under the uniform input $Re^* = 250$ with the different entrance length: (a) Ar = 2.4, (b) Ar = 6.4. Note: $W/H = 2$, where W is the width of the flow channel.

there is no flow separation in the flow sensor testing [6], which explained the behavior of the undiminished flow range in their observation. Therefore, this proposed criterion d^* based on 2D simulation will be a general guideline for the packaging design and manufacturing of micro thermal flow sensors.

However, as it is marked as a diamond symbol, the separated flow in the S-type TMCF sensor is located in the attached flow region, i.e. in the left hand of the solid line (Ar = 10). The reason for this inconsistency mainly comes from the overly simplified 2D simulation. In the experiments, the TMCF sensor is a kind of rectangular pillar stands in the center of the flow channel, which is different from Dumstorff *et al* [6] setup that the sensor span over the entire channel width. Therefore, more detailed 3D CFD simulations with the consideration of width difference between the flow channel and the sensor chip are necessary.

The in-house developed 3D simulation code (transient analysis) is based on the third-order gas-kinetic scheme in our previous papers [21, 23], which relies on the BGK model. The BGK model [24] is a simplified relaxation model for the Boltzmann equation. The Navier–Stokes equations can be derived from the BGK model by the Chapman–Enskog expansion. To achieve high accuracy, the third-order WENO method [25, 26] is used for spatial reconstruction. A time-dependent gas-distribution function can be obtained at the cell interface, which provides the numerical fluxes in the finite volume scheme. The temporal accuracy is achieved by integrating the time-dependent gas distribution function, without using the Runge–Kutta method. Compared with the second-order center scheme in the CFD-ACE + simulation, the employment of third-order scheme would prevent the issue of high dense mesh cells in the CFD models and make the 3D simulation time becomes acceptable.

The 3D CFD simulations were performed with four cores of Intel Core i7-4770 CPU @ 3.40 GHz. In the computation, the non-uniform mesh with $260 \times 150 \times 120$ mesh points was used. The mesh sizes around the sensor are $\Delta x = 1/80$, $\Delta y = 1/300$ and $\Delta z = 1/60$. Each simulation case last for enough time to make sure that the static state of fluid flow is achieved. Similar to the 2D simulations, the channel aspect ratio Ar has a profound impact on the flow pattern (left side plotted) over the S-type sensor as shown in figure 11. The shorter Ar will lead to an easily generated flow separation with the lower speed input flow.

A series of 3D simulations were conducted, as compared to the 2D counterparts, the in-house-developed 3D code shows
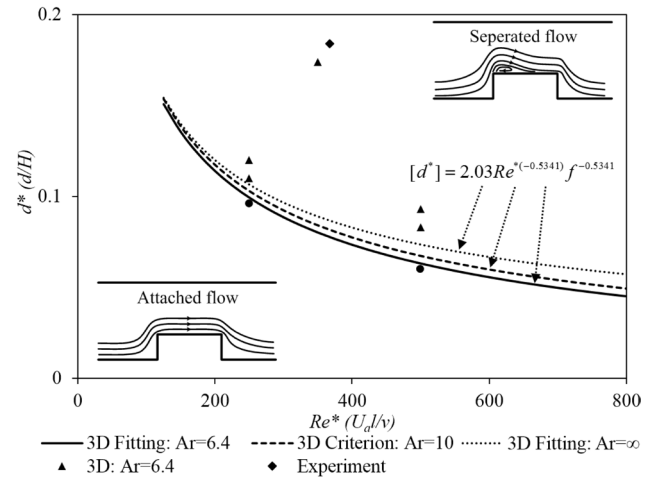

Figure 12. 3D Flow regime map indicating the separated flow over the TMCF sensor chip based on the normalized parameters d^* and Re^* with the different Ar; attached flow (circles), separated flow (triangles). Note: $W/H = 2$.

a much stricter criterion for our experimental condition, as shown in figure 12 (dashed line). With a fitting factor $\varepsilon = 3$ for the general criterion of equation (11), a modified new criterion which considers both d^* and Ar, while taking the channel width ($W/H = 2$) into consideration, is introduced in equation (13). The experimental results of our TMCF sensor are marked at the upper bound of this new criterion d^* for the flow separation. It is reasonable that the experiment result is away from the new criterion since the TMCF sensors only occupied the middle region of the chip (one-third of the chip area along the x direction). Therefore, this specialized criterion d^* will be a useful guideline for the packaging design of the fabricated CMOS TMCF sensors.

$$[d^*] = d^*/\varepsilon = 2.03Re^{*(-0.5341)}f^{-0.5341} \qquad (13)$$

Conclusion

The effect of two packaging designs, S-type and E-type, on the performance of the CMOS TMCF sensors were experimentally and numerically studied in detail. The experimental results of TMCF sensors indicated that not only the sensitivity of the S-type sensor was significantly changed, but also the input flow range as compared to the E-type was dramatically reduced from 0–11 m s^{-1} to 0–4.5 m s^{-1}. Therefore, the

packaging of the thermal flow sensor is critical to achieve a reliable and accurate flow measurement system.

To understand the physics behind the response of the two packaging designs, comprehensive 2D and 3D CFD simulations were performed. The simulation results revealed that the generated flow separation at the surface of TMCF sensors could dramatically reduce the sensor performance, in particular on the sensor's flow range. Based on the CFD model, a flow regime map (protrusion d^* versus reduced chip Reynolds number Re^*) under different channel aspect ratio Ar was constructed to serve as a useful guideline for designing a well-packaged flow sensor system, where the criterion for the flow separation over the CMOS TMCF sensor is determined as $[d^*] = 2.03\ Re^{*(-0.5341)}f^{(-0.5341)}$. More detailed CFD simulations with coupled fluid mechanics and heat transfer will be conducted in the future.

Acknowledgments

References

[1] van Putten A F and Middelhoek S 1974 Integrated silicon anemometer *Electron. Lett.* **21** 425–6

[2] Silvestri S and Schena E 2012 Micromachined flow sensors in biomedical applications *Micromachines* **3** 225–43

[3] Nguyen N 1997 Micromachined flow sensors—a review *Flow Meas. Instrum.* **8** 7–16

[4] Wang Y *et al* 2009 MEMS-based gas flow sensors *Microfluid. Nanofluid.* **6** 333–46

[5] Kuo J T, Yu L and Meng E 2012 Micromachined thermal flow sensors—a review *Micromachines* **3** 550–73

[6] Dumstorff G, Brauns E and Lang W 2015 Investigations into packaging technology for membrane-based thermal flow sensors *J. Sens. Sens. Syst.* **4** 45–52

[7] Xu W, Gao B, Chiu Y and Lee Y K 2016 Packaging effect on the flow separation of CMOS thermoresistive micro calorimetric flow sensors *11th Annual IEEE Int. Conf. on Nano/Micro Engineered and Molecular Systems* (https://doi.org/10.1109/NEMS.2016.7758201)

[8] Baltes H, Brand O, Fedder G K, Hierold C, Korvink J G and Tabata O 2008 *CMOS-MEMS: Advanced Micro and Nanosystems* (New York: Wiley)

[9] Hagleitner C, Hierlemann A, Lange D, Kummer A, Kerness N, Brand O and Baltes H 2001 Smart single-chip gas sensor microsystem *Nature* **414** 293–6

[10] Piotto M, Dei M, Butti F, Pennelli G and Bruschi P 2012 Smart flow sensor with on-chip CMOS interface performing offset and pressure effect compensation *IEEE Sens. J.* **12** 3309–17

[11] Bruschi P, Nurra V and Piotto M 2008 A compact package for integrated silicon thermal gas flow meters *Microsyst. Technol.* **14** 943–9

[12] Mayer F, Paul O and Baltes H 1995 Influence of design geometry and packaging on the response of thermal CMOS flow sensors *8th Int. Conf. on Solid-State Sensors and Actuators, 1995 and Eurosensors IX Transducers '95* vol 1 pp 528–31

[13] Makinwa K A and Huijsing J H 2002 A smart wind sensor using thermal sigma-delta modulation techniques *Sensors Actuator* A **97** 15–20

[14] Potter M C, Wiggert D C and Ramadan B H 2011 *Mechanics of Fluids* (Stamford, CT: Cengage Learning)

[15] Xu W, Song K, Ma S, Chiu Y and Lee Y K 2014 One dimensional model of thermoresistive micro calorimetric flow sensors for gases and liquids considering Prandtl number effect *18th Int. Conf. on Miniaturized Systems for Chemistry and Life Sciences (MicroTAS2014)* pp 2333–5

[16] Xu W, Song K, Ma S, Gao B, Chiu Y and Lee Y K 2016 Theoretical and experimental investigations of thermoresistive micro calorimetric flow sensors fabricated by CMOS MEMS technology *J. Microelectromech. Syst.* **25** 954–62

[17] Tseng S H, Hung Y J, Juang Y Z and Lu M S 2007 A 5.8 ghz vco with cmos-compatible mems inductors *Sensors Actuator* A **139** 187–93

[18] Xu W, Gao B, Ma S, Zhang A, Chiu Y and Lee Y K 2016 Low-cost temperature-compensated thermoresistive micro calorimetric flow (T^2MCF) sensor by using 0.35 μm CMOS MEMS technology *29th IEEE Int. Conf. on Micro Electro Mechanical Systems (IEEE MEMS '16)* pp 189–92

[19] Elwenspoek M and Wiegerink R 2001 *Mechanical Microsensors* (Berlin: Springer) pp 153–208

[20] Holman J P 2002 *Heat Transfer* (New York: McGraw-Hill) pp 212–27

[21] Xu K 2001 A gas-kinetic BGK scheme for the Navier–Stokes equations and its connection with artificial dissipation and Godunov method *J. Comput. Phys.* **171** 289–335

[22] Xu K 2015 *Direct Modeling for Computational Fluid Dynamics: Construction and Application of Unified Gas Kinetic Schemes* (Singapore: World Scientific)

[23] Pan L and Xu K 2015 A third-order gas-kinetic scheme for three-dimensional inviscid and viscous flow computations *Comput. Fluids* **119** 250–60

[24] Bhatnagar P L, Gross E P and Krook M 1954 A model for collision processes in gases I: small amplitude processes in charged and neutral one-component systems *Phys. Rev.* **94** 511–25

[25] Liu X D, Osher S and Chan T 1994 Weighted essentially non-oscillatory schemes *J. Comput. Phys.* **115** 200–12

[26] Jiang G S and Shu C W 1996 Efficient implementation of weighted ENO schemes *J. Comput. Phys.* **126** 202–28